Charge-Transfer Promoted Fixation of Glyphosate on TiO_2 - a Multiscale Approach

Filippo Balzaretti,*[a] Maria von Einem,[a] Luca Gerhards,[b] Wilke Dononelli,[a,e] Tim Stauch,[c,d,e] Thorsten Klüner,[b] and Susan Köppen*[a,d,e]

1 Introduction

It is of scientific evidence that our planet is suffering of aquatic pollution as never before. Although in recent years the main public attention has been focusing on the enormous presence of (micro)plastics in water[1–4], contamination due to organic agents remains one of the most urgent environmental challenges of our time[5–7]. Among the contaminants of organic nature, pesticides and herbicides widely used in the agriculture sector are found in our drinking water at relatively high concentrations[8–10]. Whenever a compound is released on plants or directly onto the soil, in fact, a major part of it percolates in the ground right underneath. This results not only in the contamination of the humus, but also in the nesting of these products within the underlying aquifers. Thus, over time, these compounds reach our oceans, our rivers and, consequently, our sinks at home.

The molecule of glyphosate (GGG) represents one of the most controversial issues belonging to this category. This crop-dessiccant is a non-selective organophosphate that, once discovered in 1970[11], had immediately success. The agricultural products used until then were considered more harmful and less efficient when compared to GGG, which represented instead an appealing alternative. Articles and reviews of that time started praising it, focusing on the understanding of its incredible properties rather than on possible damages to human health[12–15]. For example, the product seems to have a relatively low penetration in the soil, limited to a depth at around 15 centimeters and rarely lower[16–18]. Moreover, GGG would be naturally degraded through the action of certain subsurface bacteria that decrease the likelihood of its residues reaching ground waters[18–21]. Despite the points in favour of its usage, most of the scientific opinion believes in the dangerousness of GGG[22–24]. Major concerns regard diseases of the endocrine system, epilepsy and neurological issues[24–26]. Above all, the most fought diatribe is whether or not this herbicide can cause carcinogenic effects in humans[27]. Given its enormous controversy, the last approval of GGG among Europe was renewed for only 5 years and a new assessment will take place already in 2022[28].

The degradation process of this crop-desiccant has been the subject of intense study. In soil, GGG follows mainly two pathways of unfolding[21,29–31]. The first, well recognized reaction is the one that produces *aminomethylphosphonic acid* (AMPA) and *glycolic / glyoxylic acid*. This degradation happens when the N-C bond close to the carboxyl group of GGG gets cleaved. The second process results into *sarcosine* and *orthophosphate*, involving the unfolding of the P-C bond instead. In water, it was experimentally suggested that GGG follows a hydrolytic decomposition[29,32], highlighting H_2O molecules as active participants in the process of degradation. It was found that, at temperatures raging between 340 - 350 K and pH values of 6.5 - 7.5, GGG shows a mean half-life of about 35 days. Although also in a water environment AMPA is still recognized to be as the first degradation product, Catão et al.[30] performed a Density Functional Theory (DFT) study which showed that the C-C bond would be the most likely to get broken. The reaction proposed involves one to two water molecules depending on the protonation state of GGG (e.g. its pK_s value) and results into methyl-AMPA. Through the study of the reaction barriers, the authors also suggested that such a process can occur within a photocatalytic activation. A photo-degradation of GGG is indeed a mechanism that has been experimentally observed[25,33–35] and must therefore be the target to aim for in further research. Catão's work, though, is one of the very few theoretical studies present in literature.

The interaction with semiconductors may represent the most optimal way to degrade GGG under UV light. Among them, titanium dioxide (TiO_2) is well-known to be one of the most efficient materials in terms of photocatalytic activation[36–42]. Ilina et al.[43] investigated the interaction of TiO_2-rutile and anatase nanoparticles (NPs) in water when in presence of both GGG and AMPA. After adding the two compounds together in their sample containing the NPs, they shook it by hand and let it settle for 24 h. The observations suggested that the TiO_2 NPs do contribute in the degradation of both AMPA and GGG. According to their conclusion, it was especially the phosphate group that caused the GGG molecule to steadily adsorb to the surface. Such imputation was already attributed by several experiments for other metal oxides[24,30,44]. The carboxyl group, on the other hand, would be responsible for electronic stability. Although these results are of main interest, as stated in Ilina's work, "little is known about the role of the involved functional groups" upon degradation. This suggests that more theoretical studies are needed in order to sufficiently support the ex-

[a] *Hybrid Materials Interfaces Group, Faculty of Production Engineering, University of Bremen, Am Fallturm 1, D-28359 Bremen, Germany; E-mail: balzaretti@hmi.uni-bremen.de, koeppen@hmi.uni-bremen.de*

[b] *Theoretical Chemistry, Institute of Chemistry, Carl von Ossietzky Universität Oldenburg, Carl-von-Ossietzky-Str. 9 - 11, D-26129 Oldenburg, Germany.*

[c] *Institute for Physical and Theoretical Chemistry, University of Bremen, Leobener Straße NW2, D-28359 Bremen, Germany.*

[d] *Bremen Center for Computational Materials Science, University of Bremen, Am Fallturm 1, D-28359 Bremen, Germany.*

[e] *MAPEX Center for Materials and Processes, University of Bremen, Bibliothekstraße 1, D-28359 Bremen, Germany.*

perimental information.

In our work, we have combined different level of theories to investigate the adsorption and degradation of GGG on a surface of rutile-(110). On this slab, water molecules tend to bind molecularly with the 2-fold coordinated briding oxygen atoms of the structure[45–47]. This first layer of adsorption represents both a physical and energetical barrier for a GGG molecule to overcome, but it may also turn out in a direct recombination which activates a degradation mechanism. The methods range from classical simulations, e.g. Force Fields (FF), to *ab initio* approaches, such as DFT, and TD-DFT. In the first case, the use of newtonian equations ensured the possibility to work with a significantly large statistical sample consisting in 25 GGG molecules. This allowed us to conjecture an educated guess of what the most stable adsorption configurations should look like, which were then further investigated on the quantum mechanical level. After analyzing the adsorption energies, the electronic structure and the torsional contribution of the GGG-TiO_2 interface at its most attractive configuration, we have further suggested a mechanism of photocatalytic degradation.

2 Software and methods

2.1 Force Fields (FF) calculations

GGG - The structure of the GGG molecules has been taken from the PubCHem data base (https://pubchem.ncbi.nlm.nih.gov/compound/3496). Force field parameters were generated using Antechamber, implemented in the AMBER program package[48] based on the AMBER99SB force field. The partial charges were calculated with GAUssian98 (6-31G*)[49] and are adjusted according to the RESP scheme common for AMBER force fields. For the following simulations the charge of the GGG was set to -2e.

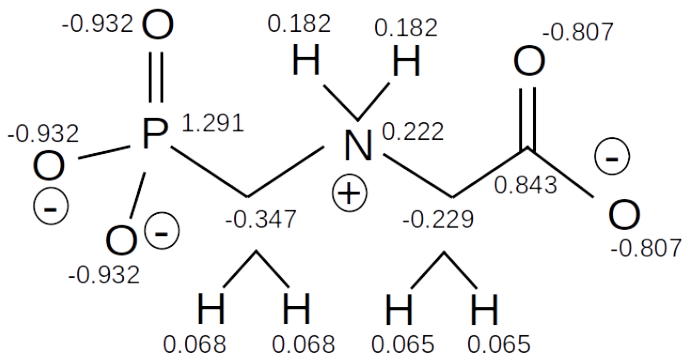

Fig. 1 RESP partial charges of GGG atoms calculated for the total molecular charge of -2e.

TiO_2 - The x-y-dimension of the rutile-(110) slab is a 10×7 repetition of the optimized unit cells of 8.90×13.19 Å^2 from Balzaretti et al.[47] and will be periodically repeated along that plane to mimic an infinite surface structure. In z-direction the slab model is 6 layers high and forms the interface to the solvated environment with the GGG molecules at the top and bottom.

System - The simulation cell of $89.03 \times 92.32 \times 125.00$ Å^3, corresponds exactly to the slab dimensions in the x-y direction and creates a gap in the z - direction, so that there is about 100 Angstrom solution phase between the periodic cells. We calculated a total of 2 systems with 25 GGG molecules each, pre-positioned 4 Angstroms high above the slab surface in a grid-like fashion with a spacing of about 7 Angstroms from each other. Each of the 25 molecules is rotated by 15 degree about the molecular x-axis. The two systems differ in the orientation on the titania slab. To ensure that we do not take over any influences of the starting positions when evaluating the adsorption modes, we rotated the GGG molecules by 90 degree in the second system around the z-axis.

Calculation protocol - First, the systems with 25 molecules on the titanium dioxide surface were calculated in AMBER for a few 100 ps in an implicit solvent environment (Generalized Born Model) to approximate the molecules to the surface. All further calculation steps were performed with the GROMACS program package. For this purpose, the topology and coordinate file were converted with an open source conversion script in Python (acpype.py) into the GROMACS format. The cell was filled with TIP3P water. Equilibration of the system was performed over 0.2 ns in NpT ensemble and 0.5 ns in NVT ensemble at RT using the Berendsen barostat and the V-rescale thermostat[50]. To increase the sampling of the adsorption modes, quenched annealing between 300 and 500 K of 10 cycles for 2 ns in total are added. Subsequently, each system was calculated molecularly for 110 ns with a time step of 2 fs, which we used to evaluate the adsorption modes.

2.2 Density functional theory calculations

All electronic structure calculations were performed with periodic boundary conditions in the framework of density functional theory (DFT), as implemented in the Vienna ab initio simulation package (VASP)[51]. The exchange-correlation energy was approximated using the PBE functional[52], additionally adding D3 dispersion correction[53]. The effect of the core electrons on the valence density was taken into account by means of the projector augmented wave (PAW) method[54] with an energy cutoff of 700 eV for static calculations, 400 eV in dynamical simulations and a kinetic energy cutoff of 645 eV for both. A $2\sqrt{2}x3$ repetition of a surface unit cell for rutile-(110) consisting of 6 tri-layers was used in all calculations. The bulk parameters consisted of $a = b = 4.663$Å and $c = 2.968$Å, evaluated with a $3 \times 3 \times 3$ k-point mesh[47]. In order to avoid spurious interaction of the molecules with the surface image repeated in the z direction, a vacuum slab of $z = 55$Å was used. All atoms were relaxed until the change in the Force was lower than 10^{-3} eV/Å. All calculations were performed using a Γ-point only setup, unless otherwise specified. Charge transfer has been investigated using the Bader code of Henkelmann and co-workers[55]. The effect of solvation in water was accounted for either by using an implicit solvation model as implemented in VASPsol[56–58] or with explicit water.

For ab initio molecular dynamics calculations (AIMD), the same thermodynamic ensembles used in FF calculations were taken into account. Instead of room temperature, here 320 K were chosen instead in order to avoid overstructures of liquid water, which is a known problem of GGA simulations[59]. The time step was set to

$dt = 0.5$ fs, with a rescaling temperature and corresponding sampling frequency every 25 steps. Part of the AIMD calculations were performed adding water molecules explicitly. The procedure of initializing the solvent positions can be found in ref[47].

Density of states (DOS) calculations were also carried out, for which a $9 \times 9 \times 1$ k-points mesh was chosen. They were carried out according to the above setup to be further analyzed using the free software of *vaspkit*[60] together with the *VASPMO* tool[61].

2.3 Judgment of Energy DIstribution (JEDI)

JEDI is a quantum chemical tool to analyze the distribution of strain energy in mechanically deformed molecules.[62–64] Based on the harmonic approximation, the strain in each internal coordinate of the deformed molecule, i.e. in each bond, bending and torsion, is quantified. Visualization is achieved with VMD[65] by mapping the strain energies in each internal coordinate onto the bonds. Custom python routines were used for this purpose. JEDI requires the geometry and the Hessian matrix of the investigated molecule in the relaxed state as well as a mechanically strained geometry. In the present case, the relaxed geometry was generated by optimizing GGG freely in solution, whereas the geometry of GGG adsorbed on the surface was taken as the mechanically strained structure.

2.4 Cluster model simulations

For the calculation of the photocatalytic properties of adsorbed GGG an embedded cluster model approach for the description of the surface was used. The cluster model was generated from cell parameters and atomic positions from calculations with periodic boundary conditions at the PBE level of theory (see above). The cluster model is divided into three different regions. The first central part is the cluster of the rutile-(110) surface which consists of a charged $Ti_{27}O_{54}[O_{34}]^{68-}$ fragment where every Ti-atom is fully chemically coordinated by O-atoms in order to avoid artificial dangling bonds that will lead to unrealistic excitation. The cluster model is embedded in a point charge field (PCF) with 71247 point charges that are arranged according to the lattice parameters. For the Ti-atoms a point charge value of +2 and for the O-atoms a value of -1 was selected in order to account for the long-term Coulomb potential. Point charge values that reflect the charge of the atoms rather than the oxidation state are used.[?] To prevent overpolarization of the cluster model a boundary region between the cluster and the PCF with 113 effective core potentials (ECP) that are located at the Ti-atom positions in the PCF near the cluster model were included.[66] In the supporting information a detailed description of the cluster model is provided. All calculations were performed using the Orca program package in version 4.2.[67] The pob-TZVP basis set was selected for the description of the cluster and adsorbate atoms.[68] For the ECP the SDD potentials, included in the Orca program package, were used. All calculations were performed by using the PBE exchange correlation functional with D3 dispersion correction. Geometry optimization of the adsorbate was performed by relaxing all adsorbate atoms and 14 surface atoms that are directly located near the adsorbate (see supporting information). Time-dependent density functional (TD-DFT) simulations were performed using an auxillary basis set (Def2-SVP/C) and the RIJCOSX approximation.[69]

Molecular snapshots are illustrated with *Visual Molecular Dynamics* (VMD)[65].

3 Results

3.1 Force Fields statistical sampling

Two systems with 25 GGG molecules respectively are evaluated in terms of possible adsorption modes. In total 47 of the 50 analysed molecules are found to be directly adsorbed on the titania surface, whereas two molecules are indirectly adsorbed on top of the first water layer. In the following discussion these two molecules are specified as not adsorbed (n. ad.) in figure 2, as they have no specific mode to the surface. The GGG molecule is very rich in charged functional groups. At each end of the molecule, either a phosphate group or a carboxylate group are known to show high attraction to titania surfaces[?]. Therefore, we proposed two different adsorption modes 2, namely a bidentated or monodentated configuration. At the bidentated configuration, both ends of the molecule are adsorbed to surface titanium atoms either within the same row (Bid. ||) or at different sides of a bridging oxygen atom (Bid. $\perp$). For a monodentated configuration, we differentiate between the phosphate group (P) end or the carboxylic group (C) end towards the surface. Since the central amino group can attribute to the adsorption modes, we specified between pure ending adsorptions, namely P-vertical (P-ver.) and C-vertical (C-ver.), and modes where the amino group is involved, namely P-step and C-step. In figure 2C the distribution of these six modes is plotted as a histogram evaluated for each of the 50 molecules in a total simulation time of 110 ns and a sampling frequency of 10 ps.

The bidentated modes are the dominating ones, whereas the monodentated modes have only minor contributions. At the bidentated modes, the bidentate-$\perp$ configuration with almost half of the molecules bond in that mode is identified as the most favorable adsorption mode. In figure 2D the time evolution of the adsorptions modes of 25 GGG molecules are plotted for a time line of 1 ns with a sampling frequency of 1 ps. It is clearly visible that bidentated modes stay stable during the simulation, whereas the P-vertical configuration tends to be converted into a bidentated mode. On the contrary, the C-vertical configuration does not change its orientation during the simulation and rather stays in its vertical orientation. We assume that for the P-vertical configuration the addition of the central amino contacts is more probable which leads in most cases at the end to a bidentated mode. For this reason, almost no step configurations are present in the histogram in figure 2C.

3.2 Adsorption at the quantum level

The six specified configurations analysed with the FF approach were positioned on the DFT rutile-(110) slab model, accordingly. After having performed a geometry optimization, we evaluated

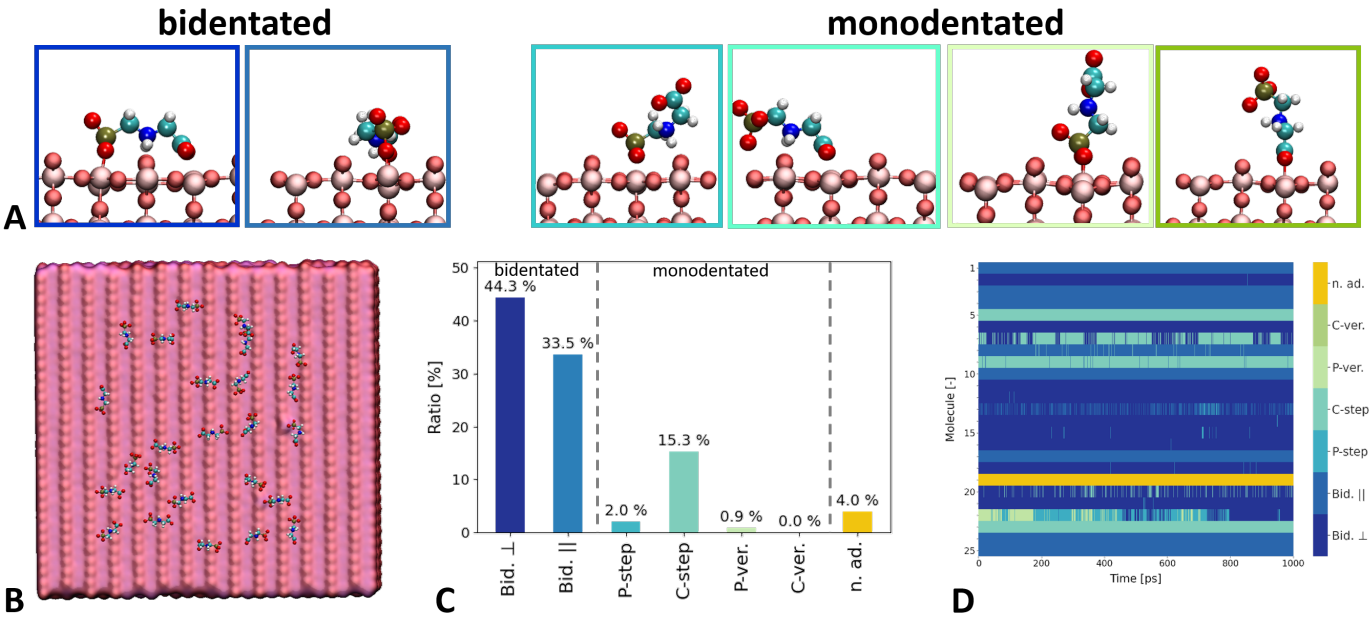

Fig. 2 Adsorption configurations of GGG on rutile-(110): (A) Snapshots of possible adsorption configurations sorted by bidentated and monodentated modes are illustrated from left to right: Bid. ⊥, Bid. || and P-step, C-step, P-ver. and C-ver., (B) representative snapshot of 25 GGG molecules after 100 ns classical molecular dynamics simulations, (C) distribution of adsorption modes listed in A, evaluated from 50 GGG molecules for a simulation time of 110 ns with a sampling frequency of 10 ps, (D) time evolution of the adsorption modes of 25 molecules for a duration of 1 ns with a sampling frequency of 1 ps.

their adsorption energy through the following formula:

$$\Delta E_{\text{ads}} = E_{\text{GGG distant from rutile}} - E_{\text{GGG on rutile}} \quad (1)$$

The term $E_{\text{GGG distant from rutile}}$ refers to the system with GGG positioned at a distance of 14Å from rutile. The second energy, $E_{\text{GGG on rutile}}$, belongs instead to the molecule once adsorbed at the surface. The GGG model used in $E_{\text{GGG distant from rutile}}$ was previously optimized in a vacuum cell of the same size by a global minimum search procedure, reproducing its gas phase configuration. This, when inserted in the simulation cell at the distance of 14Å from the slab, its structure did not show any major changes. The reader should be aware that a classical way of evaluating adsorption energies would be with the two separated terms $E_{\text{GGG}} + E_{\text{rutile}}$ instead. Due to the charged background in our system, though, the use of these two factors would need an additional term of charge correction, say E_{corr}. With our approach, we directly estimate that $E_{\text{GGG distant from rutile}} \approx E_{\text{GGG}} + E_{\text{rutile}} + E_{\text{corr}}$. The adsorption energies are reported in the first line of Tab. 1.

As expected from our classical MDs, the bidentate-⊥ structure proved to lead the highest attraction. Monodentate configurations driven by the phosphate group follow immediatly after. Despite this, their presence in our previous FF simulations has a very low rate. This is due to the fact that once bound to the surface, for the phosphate group it is difficult to detach from it. The molecule, hence, starts to oscillate back and forth due to the entropy of the system and forms the bidentate-⊥, bidentate-|| or, more rarely, the P-step structure. On the other hand, both arrangements based on carboxylic moiety, showed the lowest adsorption energies. In this case, it is not straightforward to move from the C-vertical or C-step configuration into a bidentate one and, therefore, are found in our classical MDs with a minor presence.

When GGG adsorbs on rutile-(110), the charge of the formally two fold negatively charged GGG is partially transferred to the d-band of the Ti atoms of the rutile surface. The Bader net atomic charges of the six configurations are listed in the second line of Tab. 1). In case of the bidentate adsorption modes, the charge located at the GGG reduces to 1. This can be interpreted as one electron transferred from the highest occupied molecular orbital of GGG to the d-band of Ti as discussed in more detail in section 3.3.

Due to its prominent adsorption energy and charge transfer to the surface, we decided to carry on all of our further investigations on the bidentate-⊥ structure only. In order to analyze in more detail the charge transfer for the most dominant bidentate-⊥ adsorption mode, its electron density difference was evaluated. This is shown in Fig. 3, integrated for the y-direction. It can be seen that not only the oxygen atoms of the phosphate and carboxylic groups form a bond to the closest five fold coordinated Ti atoms, but in addition a hydrogen bond is formed between the hydrogen of the amino group to bridging oxygen atoms of the rutile-(110) surface. The formation of these four bonds and two additional hydrogen bonds leads to a weakening of the P-C and C-C bonds in GGG. This indicates that, potentially, the two bonds may break in a degregation process induced through adsorption at the surface.

To observe whether the bidentate-⊥ configuration was thermodynamically stable also in DFT, two AIMDs at 320 K were performed. The first one was carried out with an implicit solvent only and lasted for 8.4 ps. Here, the carboxyl group left its adsorption

Table 1 Adsorption energies and Bader net atomic charges of the optimized structures of GGG on rutile-(110)

	Bid. ⊥	Bid. ||	P-step	C-step	P-vert.	C-vert
ΔE_{ads}/eV	−3.06	−2.48	−2.92	−1.67	−2.62	−1.94
Bader chg. /e	−1.12	−1.10	−1.26	−1.33	−1.25	−1.49

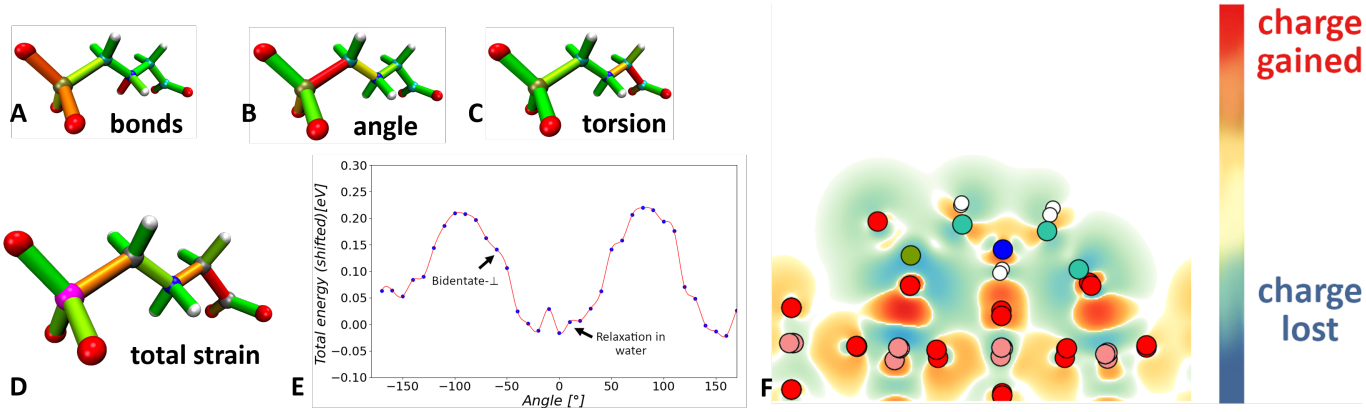

Fig. 3 Analysis of the ⊥ bidentated adsorbed configuration of GGG on on Rutile (110): the strain of (A) bonds, (B) angles and (C) torsions has been analysed via JEDI and is summed up in (D). The color code from no strain (green) to highest strain contribution (red) is plotted on the corresponding bonds. (E) The significant part of the strain in the adsorbed molecule is in the torsional motion of the C -C bond at the carboxyl end of the molecule which rotates by 60from the equilibrated structure in solution to reach the optimal adsorption mode. (F) The differences of the Bader charges are plotted for the ⊥ bidentated adsorbed molecule. Red areas indicate regions with increased electron density and blue areas with decreased electron density.

position heading toward the vacuum after 1.5 ps and the P-step configuration was then observed. Right afterward, also the amine group slacked the attraction to rutile, and the structure ended up being in the P-vertical one. In the second case, the vacuum box was filled with H_2O molecules. Due to the expensive simulation time, the calculation lasted for 2.4 ps only. This time, the bidentate-⊥ structure did not leave rutile. This suggests that the presence of water in the system is an active element in maintaining the arrangement, as it represents barrier not possible to overcome at such a temperature.

Finally, the structural deformations of bidentate-⊥ with its resulting strain was investigated by terms of JEDI analysis[62–64]. Based on our calculations, adsorption leads to a build-up of 38.5 kcal/mol strain in GGG, which is overestimated by JEDI by only 10%, justifying the use of the harmonic assumption. Approximately half of this strain energy is stored in the torsional degree of freedom around the C-C bond of GGG (Figure **??**), whereas a smaller amount of strain is also stored in the region around the P-C bond. It must be noted, however, that the relaxed structure, which serves as a reference in the JEDI analysis, is not the global conformational minimum, but rather the local torsional minimum closest to the adsorbed bidentate geometry. Hence, the real strain energy due to adsorption of GGG is higher. Nevertheless, one can conclude that the energy gained through adsorption of GGG in the bidentate conformation needs to overcompensate the strain energy in GGG (38.5 kcal/mol) and that this strain is stored predominantly in the torsion around the C-C bond. In past works, it has been found that torsional motions can weaken chemical bonds by preconditioning them for rupture.[70] Therefore, adsorption of GGG on TiO_2 holds some promise for degradation of this pollutant.

The same result of stored strain in the C-C bond was confirmed by a further analysis using DFT calculations. The GGG molecule, in its bidentate-⊥ configuration, was grabbed out from the rutile surface and embedded in an explicit water solvent. Through a new AIMD at 320 K with a duration of 2.5 ps, the structure dynamically relaxed over time until it reached thermodynamic equilibrium. At this point, the principal bonds and dihedral angles within it were measured, averaged along the last picosecond of simulation time. By evaluating the differences between these averages and the respective values of the static bidentate-⊥ at the surface, we were able to understand where the largest changes occurred. Regarding the major bonds (starting from the phosphate group toward the carboxyl group) P-C, C-N, N-C, and C-C, no significant changes were detected. Each of them, in fact, showed a difference of less than 0.03Å. The dihedral angles, indices of torsion, also remained fairly stable (differences of less than 8°) except for one case. This was precisely the dihedral involving the C-C bond, calculated from the N atom to one of the two O atoms of the carboxyl group bound to the surface (dihedral N-C-C-O). In it, a difference of about 54° was measured. In order to understand how much strain corresponded to the torsion in the C-C bond, we performed a rotation along its axis. Based on a 10° step, the energy was calculated each time using a simple Single Point Calculation (SPC). The results are shown in Fig. **??**. The configuration corresponding to 0 deg is that of dynamic relaxation in explicit solvent. As can be observed, it corresponds to a minimum of the strain in the bond. Looking instead the angle formed in the bidentate-⊥ structure, we see that we are close to a point of maximum. Thus, when the molecule approaches the surface, it is found to have a C-C bond with very high strain. This result confirms that of the JEDI analysis.

3.3 Photocatalytic perspectives

In order to investigate the photocatalytic behavior and the accompanying destabilization of bonds in the bidentate-⊥ structure, the DOS of the adsorbed system has been compared to the pristine as shown in Fig. 4. A significant reduction of the band gap is induced

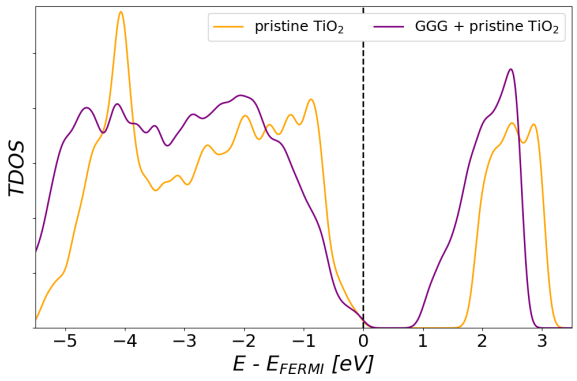

Fig. 4 Total density of states (DOS) of the pristine rutile-(110) surface (orange) with and without adsorption (purple). In the second case, the GGG atoms were also taken into account. The band gap shifts from 1.75 eV to 1.17 eV upon adsorption, leading to a higher probability of photocatalytic activation.

by the adsorption process of GGG leading to a overall band gap of 1.17 eV compared to the band gap of 1.75 eV for the pristine system. Note that the underestimation of the band gap is a well known behavior, when the PBE functional is used[71,72]. Consid-

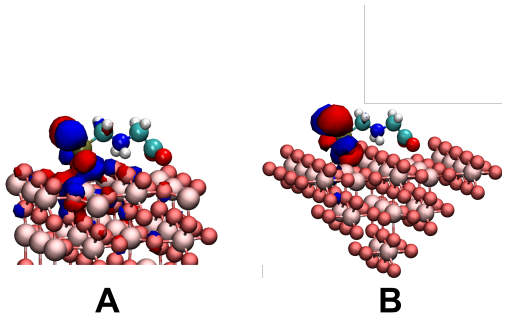

Fig. 5 Important crystalline orbital at the Gamma-point of periodic boundary condition simulation A in comparison to the cluster model HOMO B. (isovalue 0.015 e/Å^3)

ering the crystalline orbitals near the Fermi energy, a hybridization between the orbitals of GGG and the surface band arises (Fig. 5, A). Here, the previously discussed charge transfer of the adsorbate into the surface can be substantiated. The strong localization at the phosphate group indicates a destabilization of the P-C bond after photo-induced excitation. Considering the virtual bands of TiO_2 indicates that an excitation into the unoccupied Ti-d-bands form the occupied hybridization bands might occur. To simulate the electronic excitation of the adsorbed system, a cluster model was constructed which shows the same properties as our periodic boundary condition calculations (5 supporting information). Here, the HOMO of the cluster model a similar structure as the crystalline orbital of our periodic calculation. In Fig. 6, a

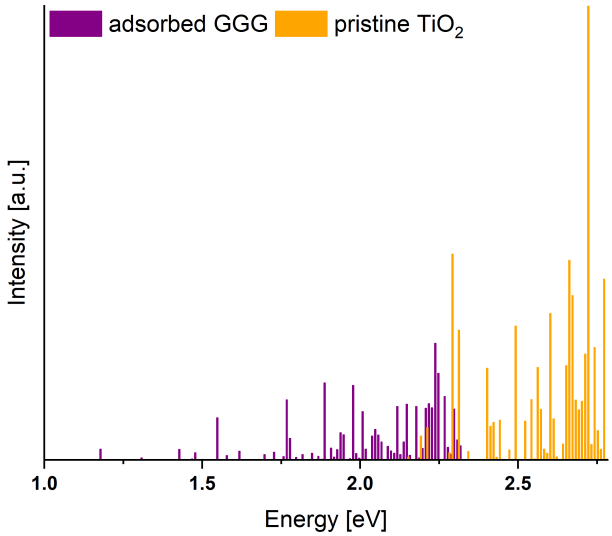

Fig. 6 TD-DFT spectra of adsorbed GGA (purple) and pristine TiO_2 (orange) on cluster model. (PBE-D3/POB-TZVP) When GGA is interacting with the surface electronic excitations at 1.14 eV can be observed while pristine TiO_2 can be excited at 2.15 eV.

comparison between the absorption spectra of the pristine rutile-(110) surface and the adsorbed GGG molecule are shown. The calculated spectra clearly indicate that the excitation energy is significantly lowered by bonding of GGG on rutile-(110). The pristine surface shows first electronic excitation at 2.15 eV, which is close to the calculated band gap of the calculations with periodic boundary conditions (1.75 eV). The gas phase molecule will be excited with higher energy, starting at 3.05 eV (c.f. SI). The adsorbed GGG shows first electronic excitations at 1.14 eV. Here again, the excitations are close to the calculated band gap of the system (see Fig. 4). Investigating the character of transitions, it becomes clear that the HOMO (highest occupied molecular orbital), which is strongly located at the phosphate group, is involved in several excitations. As previously suggested, a charge transfer into the d-bands of TiO_2 occurs leading to a even more charged adsorbate and, therefore, destabilizing the bonds in the molecule by reducing the electron density of GGG. Experimental investigations of the photocatalytic degradation proposed the breaking of the P-C bond when only involving irradiation of the system[73]. The simulations indicate that, after the photocatalyitic excitation, the P-C bond might break. This leads then to the degradation products of sacrosine and orthophosphate.

4 Conclusions

In the present manuscript we used atomistic simulation methods to investigate the adsorption of GGG on the titania rutile-(110) surface. The molecule showed a high adsorption to the surface especially in its bidentate-⊥ mode. This configuration was further investigated both in terms of charge transfer and strain analysis. In the first case a transfer of roughly one electron was observed from the functional groups binding to the surface atoms, leaving the molecule at the phosphate and carboxylic groups. This charge is distributed into the rutile's bulk, where it gets then dissipated. To get a hint on the location of the bond break, the strain analysis

identified the C-C bond as the major strain location. This presumption can not be confirmed in this work. In order to understand photocaltalytic degradation of GGG in further investigations, a cluster model was developed for TD-DFT simulations. The cluster simulations are in good agreement with the DFT simulations in terms of ground state properties (band gap and HOMO-levels) as well as geometrically optimized structures. Here not only the DOS showed a reduction of the band gap upon adsorption, but also the TD-DFT spectrum lied in the same regime. Hence, there is a high likelihood for GGG to proceed in a photocatalytic reaction.

Conflicts of interest

There are no conflicts to declare.

Acknowledgements

The work on this manuscript has been performed within the framework of the Research Training Program "Quantum Mechanical Materials Modelling - QM3" (RTG 2247) funded by the Deutsche Forschungsgemeinschaft (DFG). Furthermore, we want to thank Lucio Colombi Ciacchi, Tim Wehling and Jan Berges for fruitful discussions within that project.

5 Supporting Information

5.1 Embedded cluster model construction

For the construction of the embedded cluster model a supercell was generated using the geometrical parameter from periodic boundary condition calculations. A half sphere point charge field (PCF) was cut out of the supercell with the restriction of charge neutrality as described in literature. For the point charges in the half-sphere the values -1 and +2 where used to simulate the right long-range potential of the atoms in the TiO_2 solid. In the center of the half sphere a $Ti_{27}O_{54}[O_{34}]^{68-}$ cluster that will be treated quantum mechanically and 113 Ti atoms that are described by effective core potentials (ECP) to avoid overpolarization of the cluster model are cut out of the point charge field (Fig. 7).

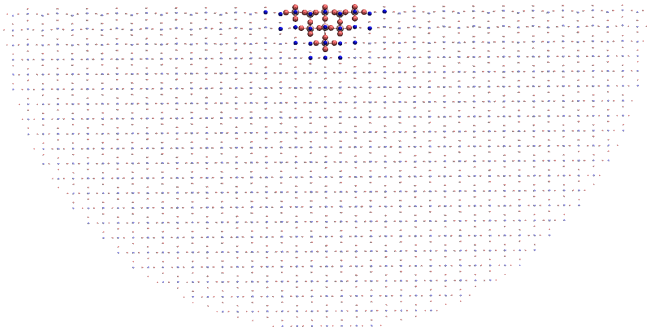

Fig. 7 Representation of embedded cluster model. In the center lies the $Ti_{27}O_{54}[O_{34}]^{68-}$ cluster surrounded by 113 ECP (blue) and 71247 PCs (transparent red and blue).

To achieve net charge neutrality of the system, the ECP atoms are divided into two separate shells where the outer shell has the same charge value as the point charges in the PCF (Ti = +2) and the inner shell additionally compensates the charge of the cluster leading to a value of +2.723 per ECP atom. The charged cluster approach is used to avoid the appearance of artificial states between the band gap that are caused by dangling bonds when using a stoichiometric cluster. For the geometrical relaxation 14 atoms of the first layer where relaxed in order to achieve a comparably similar adsorption geometry of GGG as calculated in our periodic boundary condition approach. To validate our cluster model a comparison between specific properties of the boundary calculations and the cluster model can be evaluated. Table 2 shows the band gap of the pristine surface and the geometry of the adsorbed GGG of both approaches.

As can be observed the results are in good agreement and the cluster model is capable of reproducing the electronic structure calculations with periodic boundary conditions. Therefore, the qualitative investigation of electronic excitation using the cluster model can be justified.

Notes and references

1 A. Schwarz, T. Ligthart, E. Boukris and T. van Harmelen, *Marine Pollution Bulletin*, 2019, **143**, 92–100.

2 I. E. Napper, B. F. Davies, H. Clifford, S. Elvin, H. J. Koldewey, P. A. Mayewski, K. R. Miner, M. Potocki, A. C. Elmore, A. P. Gajurel and R. C. Thompson, *One Earth*, 2020, **3**, 621–630.

3 W. Y. Chia, D. Y. Ying Tang, K. S. Khoo, A. N. Kay Lup and K. W. Chew, *Environmental Science and Ecotechnology*, 2020, **4**, 100065.

4 P. Wanner, *Chemosphere*, 2021, **264**, 128453.

5 E. Boelee, G. Geerling, B. van der Zaan, A. Blauw and A. D. Vethaak, *Acta Tropica*, 2019, **193**, 217–226.

6 A. Li, C. Kroeze, T. Kahil, L. Ma and M. Strokal, *Current Opinion in Environmental Sustainability*, 2019, **40**, 88–94.

7 G. Gomes-Silva, E. Cyubahiro, T. Wronski, R. Riesch, A. Apio and M. Plath, *Science of The Total Environment*, 2020, **730**, 138912.

8 N. Trautmann, K. Porter and R. Wagenet, 1985.

9 J. de Castro Lima, J. Labanowski, M. Bastos, R. Zanella, O. Prestes, J. Vargas, L. Mondamert, E. Granado, T. Tiecher, M. Zafar, A. Troian, T. Le Guet and D. dos Santos, *Environmental Science and Pollution Research*, 2020, **27**,.

10 M. Syafrudin, R. Ayu, A. Yuniarto, T. Hadibarata, J. Rhee, W. Al-Onazi, T. Algarni, A. Almarri and A. Al-Mohaimeed, *International Journal of Environmental Research and Public Health*, 2021, **18**, 468.

11 D. Baird, *Proceedings of the 26th North Central Weed Conference (Kansas City, USA, 7-9 December 1971)*, 1971.

12 H. Steinrücken and N. Amrhein, *Biochemical and Biophysical Research Communications*, 1980, **94**, 1207–1212.

13 M. R. Boocock and J. R. Coggins, *FEBS Letters*, 1983, **154**, 127–133.

Table 2 Comparison of band gap (pristine surface) and geometrical parameter of adsorbed GGG on TiO_2 with cluster model and periodic boundary condition

Approach	band gap [eV]	P-C[A]	N-C[A]	C-N[A]	C-C[A]
PBC	1.75	1.893	1.489	1.505	1.569
Cluster	2.147	1.942	1.497	1.507	1.578

14 C. C. Smart, D. Johänning, G. Müller and N. Amrhein, *Journal of Biological Chemistry*, 1985, **260**, 16338–16346.

15 C. S. Gasser, J. A. Winter, C. M. Hironaka and D. M. Shah, *Journal of Biological Chemistry*, 1988, **263**, 4280–4287.

16 M. Meyer, J. Frey, E. Lee, K. Kuivila and M. Sandstrom, *229th American Chemical Society National Meeting. San Diego CA, US: American Chemical Society.*, 2005.

17 H. Vereecken, *Pest management science*, 2005, **61**, 1139–51.

18 A. Cerdeira and S. Duke, *GM crops*, 2010, **1**, 16–24.

19 R. Haney, S. Senseman and F. Hons, *Journal of Environmental Quality*, 2002, **31**, 730–735.

20 M. Grube, U. Kalnenieks and O. Muter, *Ecotoxicology and Environmental Safety*, 2019, **173**, 373–380.

21 S. Singh, V. Kumar, J. Gill, S. Datta, S. Singh, V. Dhaka, D. Kapoor, A. Wani, D. Dhanjal, M. Kumar and J. Singh, *International Journal of Environmental Research and Public Health*, 2020, **17**,.

22 M. Cuhra, T. Bøhn and P. Cuhra, *Frontiers in Bioscience*, 2016, **4**,.

23 R. Mesnage, C. Benbrook and M. Antoniou, *Food and Chemical Toxicology*, 2019, **128**,.

24 K. Sen, in *5 - A comprehensive review of glyphosate adsorption with factors influencing mechanism: Kinetics, isotherms, thermodynamics study*, 2020, pp. 93–125.

25 M. Silva and J. Baltrusaitis, *Journal of Hazardous Materials Letters*, 2021, **2**, 100012.

26 S. X. Naughton and A. V. Terry, *Toxicology*, 2018, **408**, 101–112.

27 J. Tarazona, D. Court Marques, M. Tiramani, H. Reich, R. Pfeil, F. Istace and F. Crivellente, *Archives of toxicology*, 2017, **91**,.

28 P. Kudsk and S. K. Mathiassen, *Weed Science*, 2020, **68**, 214 – 222.

29 J. Schuette, *Environmental Monitoring Pest Management, Department of Pesticide Regulation, Sacramento*, 1998.

30 A. Catão and A. López-Castillo, *Environmental Science: Processes Impacts*, 2018, **20**,.

31 S. O. Duke, *Weed Science*, 2020, **68**, 201–207.

32 W. Kollman and R. Segawa, *Department of Pesticide Regulation: Environmental Protection Agency, Sacramento, California*, 1995.

33 Y. Yang, Q. Deng, W. Yan, C. Jing and Y. Zhang, *Chemical Engineering Journal*, 2018, **352**, 581–589.

34 Z. Zhang, Z. Ouyang, J. Yang, L. Yanjun, C. Yang and Z. Dang, *Environmental Chemistry Letters*, 2019, **17**,.

35 P. Garcia-Muñoz, W. Dachtler, B. Altmayer, R. Schulz, D. Robert, F. Seitz, R. Rosenfeldt and N. Keller, *Chemical Engineering Journal*, 2020, **384**, 123315.

36 S. Chen and Y. Liu, *Chemosphere*, 2007, **67**, 1010–7.

37 V. Augugliaro, M. Bellardita, V. Loddo, L. Palmisano and S. Yurdakal, *Journal of Photochemistry and Photobiology C: Photochemistry Reviews*, 2012, **13**, 224–245.

38 M. Visa, L. Isac and A. Duta, *Applied Surface Science*, 2015, **339**,.

39 M. Cruz, C. Gomez, C. Durán-Valle, L. Pastrana Martinez, J. Faria, A. Silva, M. Faraldos and A. Bahamonde, *Applied Surface Science*, 2015, **416**,.

40 K. Umar, A. Aris, H. Ahmad, T. Parveen, J. Jaafar, Z. Abdul Majid, V. B. R. A and J. Talib, *Journal of Analytical Science and Technology*, 2016, **7**,.

41 Y. Yang, Q. Deng and Y. Zhang, *Chemical Engineering Journal*, 2018, **360**,.

42 G. Rangarajan, G. Kannappan Panchamoorthy, V. Nagarajan, A. Krishnan and M. R., *Journal of Environmental Management*, 2020, **270**,.

43 S. Ilina, P. Ollivier, D. Slomberg, N. Baran, A. Pariat, N. Devau, N. Kast, M. Scheringer and J. Labille, *Environ. Sci.: Nano*, 2017, **4**,.

44 M. S. Caetano, T. C. Ramalho, D. F. Botrel, E. F. F. da Cunha and W. C. de Mello, *International Journal of Quantum Chemistry*, 2012, **112**, 2752–2762.

45 Z.-Y. Zhao, *The Journal of Physical Chemistry C*, 2014, **118**, 4287–4295.

46 L. Agosta, E. G. Brandt and A. P. Lyubartsev, *The Journal of Chemical Physics*, 2017, **147**, 024704.

47 F. Balzaretti, V. Gupta, L. C. Ciacchi, B. Aradi, T. Frauenheim and S. Köppen, *Water reactions on reconstructed rutile TiO_2: a DFT / DFTB approach*, `arXiv:2102.02725`, 2021.

48 J. A. Maier, C. Martinez, K. Kasavajhala, L. Wickstrom, K. E. Hauser and C. Simmerling, *Journal of Chemical Theory and Computation*, 2015, **11**, 3696–3713.

49 M. J. Frisch, G. W. Trucks, H. B. Schlegel, G. E. Scuseria, M. A. Robb, J. R. Cheeseman, G. Scalmani, V. Barone, G. A. Petersson, H. Nakatsuji, X. Li, M. Caricato, A. V. Marenich, J. Bloino, B. G. Janesko, R. Gomperts, B. Mennucci, H. P. Hratchian, J. V. Ortiz, A. F. Izmaylov, J. L. Sonnenberg, D. Williams-Young, F. Ding, F. Lipparini, F. Egidi, J. Goings, B. Peng, A. Petrone, T. Henderson, D. Ranasinghe, V. G. Zakrzewski, J. Gao, N. Rega, G. Zheng, W. Liang, M. Hada, M. Ehara, K. Toyota, R. Fukuda, J. Hasegawa, M. Ishida, T. Nakajima, Y. Honda, O. Kitao, H. Nakai, T. Vreven, K. Throssell, J. A. Montgomery, Jr., J. E. Peralta, F. Ogliaro, M. J. Bearpark, J. J. Heyd, E. N. Brothers, K. N. Kudin, V. N. Staroverov, T. A. Keith, R. Kobayashi, J. Normand, K. Raghavachari, A. P. Rendell, J. C. Burant, S. S. Iyengar, J. Tomasi, M. Cossi, J. M. Millam, M. Klene, C. Adamo, R. Cammi, J. W. Ochterski, R. L. Martin, K. Morokuma, O. Farkas, J. B. Foresman and D. J. Fox, *Gaussian~16 Revision C.01*, 2016, Gaussian Inc. Wallingford CT.

50 M. J. Abraham, D. van der Spoel, E. Lindahl, B. Hess and the GROMACS development team, *GROMACS User Manual version 2016.4*, 2017.

51 G. Kresse and J. Furthmüller, *Phys. Rev. B*, 1996, **54**, 11169–11186.

52 J. P. Perdew, K. Burke and M. Ernzerhof, *Phys. Rev. Lett.*, 1996, **77**, 3865–3868.

53 S. Grimme, J. Antony, S. Ehrlich and H. Krieg, *The Journal of Chemical Physics*, **132**, year.

54 G. Kresse and D. Joubert, *Phys. Rev. 59*, 1999, **59**, 1758–1775.

55 G. Henkelman, A. Arnaldsson and H. Jonsson, *Computational Materials Science - COMPUT MATER SCI*, 2006, **36**, 354–360.

56 K. Mathew, V. S. C. Kolluru and R. G. Hennig, *VASPsol: Implicit solvation and electrolyte model for density-functional theory*, `https://github.com/henniggroup/VASPsol`, 2018, `https://github.com/henniggroup/VASPsol`.

57 K. Mathew, R. Sundararaman, K. Letchworth-Weaver, T. A. Arias and R. G. Hennig, *J. Chem. Phys.*, 2014, **140**, 084106.

58 K. Mathew, V. S. C. Kolluru, S. Mula, S. N. Steinmann and R. G. Hennig, *J. Chem. Phys.*, 2019, **151**, 234101.

59 S. Yoo, X. C. Zeng and S. S. Xantheas, *The Journal of Chemical Physics*, 2009, **130**, 221102.

60 V. Wang, N. Xu, J. C. Liu, G. Tang and W.-T. Geng, 2020.

61 Y. Wang, 2020.

62 T. Stauch and A. Dreuw, *J. Chem. Phys.*, 2014, **140**, 134107.

63 T. Stauch and A. Dreuw, *J. Chem. Phys.*, 2015, **143**, 074118.

64 T. Stauch and A. Dreuw, *Acc. Chem. Res.*, 2017, **50**, 1041–1048.

65 W. Humphrey, D. A. and S. K., *Journal of Molecular Graphics*, 1996, **14**, 33 – 38.

66 D. Berger, A. J. Logsdail, H. Oberhofer, M. R. Farrow, C. R. A. Catlow, P. Sherwood, A. A. Sokol, V. Blum and K. Reuter, *The Journal of chemical physics*, 2014, **141**, 024105.

67 F. Neese, F. Wennmohs, U. Becker and C. Riplinger, *The Journal of Chemical Physics*, 2020, **152**, 224108.

68 M. F. Peintinger, D. V. Oliveira and T. Bredow, *Journal of Computational Chemistry*, 2013, **34**, 451–459.

69 A. Hellweg, C. Hättig, S. Höfener and W. Klopper, *Theoretical Chemistry Accounts*, 2007, **117**, 587–597.

70 T. Stauch and A. Dreuw, *Angew. Chem. Int. Ed.*, 2016, **55**, 811–814.

71 J. P. Perdew, *International Journal of Quantum Chemistry*, 1985, **28**, 497–523.

72 P. Deák, M. Lorke, B. Aradi and T. Frauenheim, *Journal of Applied Physics*, 2019, **126**, 130901.

73 M. Muneer and C. Boxall, *International Journal of Photoenergy*, **2008**, 197346.